Covariant Lyapunov vectors of chaotic Rayleigh-Bénard convection

M. Xu and M. R. Paul[*]

Department of Mechanical Engineering, Virginia Tech, Blacksburg, Virginia 24061, USA
(Received 30 October 2015; revised manuscript received 25 March 2016; published 10 June 2016)

We explore numerically the high-dimensional spatiotemporal chaos of Rayleigh-Bénard convection using covariant Lyapunov vectors. We integrate the three-dimensional and time-dependent Boussinesq equations for a convection layer in a shallow square box geometry with an aspect ratio of 16 for very long times and for a range of Rayleigh numbers. We simultaneously integrate many copies of the tangent space equations in order to compute the covariant Lyapunov vectors. The dynamics explored has fractal dimensions of $20 \lesssim D_\lambda \lesssim 50$, and we compute on the order of 150 covariant Lyapunov vectors. We use the covariant Lyapunov vectors to quantify the degree of hyperbolicity of the dynamics and the degree of Oseledets splitting and to explore the temporal and spatial dynamics of the Lyapunov vectors. Our results indicate that the chaotic dynamics of Rayleigh-Bénard convection is nonhyperbolic for all of the Rayleigh numbers we have explored. Our results yield that the entire spectrum of covariant Lyapunov vectors that we have computed are tangled as indicated by near tangencies with neighboring vectors. A closer look at the spatiotemporal features of the Lyapunov vectors suggests contributions from structures at two different length scales with differing amounts of localization.

I. INTRODUCTION

The complex dynamics of large spatially extended systems that are driven far from equilibrium are central to many important challenges currently facing science and technology [1], for example, the dynamics of the atmosphere and oceans [2], fluid turbulence [3], the spread of epidemics and disease [4], and the patterns that result from nonlinear interactions between chemicals in many industrial processes [5]. Many of the challenges are rooted in the fact that the dynamics of these systems are high dimensional. This makes many powerful approaches based upon the geometry of the attractor unwieldy and difficult, if not impossible, to implement.

Significant progress has been made using Lyapunov exponents and Lyapunov vectors [6,7]. The spectrum of Lyapunov exponents quantify the exponential expansion or contraction of small perturbations to the nonlinear evolution of the dynamics. Given the spectrum of Lyapunov exponents it is possible to compute the fractal dimension of the dynamics using the formula of Kaplan and Yorke [8]. The fractal dimension can provide insight into the number of chaotic degrees of freedom active in a system on average [9]. A significant advantage of this approach is that the computation of the dimension does not rely upon the geometry of the attractor and can readily scale to high-dimensional systems (cf. Ref. [10]). An important advance was the emergence of algorithms to compute the Lyapunov spectrum that used frequent Gram-Schmidt reorthonormalizations [11–13].

This approach has been applied to a range of important spatially extended systems including coupled-map lattices [14], the Lorenz-96 model [15], the Kuramoto-Sivashinsky equation [16], and Rayleigh-Bénard convection [10,17–20]. Spatially extended fluid systems with fractal dimensions as large as 50 have been explored [10]. This approach has shed new physical insights on the extensivity of chaos in large dissipative systems [14–16] by quantifying the variation of the fractal dimension with changes in the size of the system. In addition, the leading order Lyapunov vector has been used to highlight regions in the patterns where the growth of disorder is largest [10,17]. However, a significant disadvantage of this approach is that the directions of all of the Lyapunov vectors, except for the leading order vector, are lost due to the frequent reorthonormalizations.

It is well known that there exists a set of vectors intrinsic to the dynamics which satisfy the so-called Oseledets splitting [7,21] (often spelled Oseledec in the literature). These intrinsic vectors are often referred to as the characteristic or covariant Lyapunov vectors. Until recently the covariant Lyapunov vectors remained mostly a formal idea since there was not a computationally accessible approach for their calculation. Ginelli *et al.* [22], Wolfe *et al.* [23], and Pazó *et al.* [24] presented algorithms to calculate the covariant Lyapunov vectors that are computationally accessible. The covariant Lyapunov vectors have since been used to provide new physical insights into the dynamics of coupled-map lattices [22,24–27], the Lorenz-96 model [24], the Kuramoto-Sivashinsky equation [27,28], Kolmogorov flow [29], and the complex Ginzburg-Landau equation [27,28].

Knowledge of the covariant Lyapunov vectors allows one to probe fundamental features of the dynamics that until now have been inaccessible. The Lyapunov vectors with positive Lyapunov exponents correspond to the unstable manifold. Similarly, the Lyapunov vectors with negative Lyapunov exponents correspond to the stable manifold. The minimum angle between the stable and unstable manifolds can be used to quantify the degree of hyperbolicity of the dynamics. A dynamical system is hyperbolic if the stable and unstable manifolds intersect with nonzero angles (cf. Refs. [22,30]).

Many important mathematical ideas used in the study of dissipative dynamical systems, such as the shadowing theorem [31], rest upon the assumption of hyperbolicity. Although it is expected that most realistic systems are not hyperbolic this has never been quantified.

It has recently been shown that the tangent space of several dissipative dynamical systems can be split into two different

[*]mrp@vt.edu

modes called physical modes and spurious or isolated modes [28] whose categorization depend crucially upon knowledge of the angles between the covariant Lyapunov vectors. The physical modes are composed of covariant Lyapunov vectors that contain frequent tangencies. The spurious modes are composed of covariant Lyapunov vectors that do not contain any tangencies. The spurious modes are hyperbolic with respect to the physical modes and with respect to the other isolated modes. The tangencies of the physical modes allow them to interact with one another, and it has been suggested that these modes contain the fundamental features required to describe the dynamics [27]. The hyperbolicity of the spurious modes, on the other hand, makes them noninteracting with the other modes, and they are found to be rapidly decaying.

As elucidated in Ref. [27], two nondegenerate covariant Lyapunov vectors can never become exactly tangent with one another. However, the angle between them can become arbitrarily small to yield a finite probability at zero or π in their angle distribution. In our discussion, we use the term tangency to describe this situation.

Furthermore, it has been conjectured that the number of physical modes is representative of the dimension of the inertial manifold [28]. The inertial manifold has remained, until recently, a formal mathematical idea that has been difficult to quantify in practice (cf. Ref. [32]). The inertial manifold is a smooth object in phase space upon which the dynamics approach after a short initial transient. The dynamics then eventually evolve onto a global attractor that is embedded within the inertial manifold. An estimate of the global attractor dimension is given by the fractal dimension [9]. Results for several nonlinear dissipative systems have found the inertial manifold dimension to be only several times larger than the fractal dimension [27,28].

Knowledge of the dimension of the dynamics is of practical interest. The dimension is an estimate for the number of active degrees of freedom on average [9]. For example, the dimension of the inertial manifold is an estimate for the minimum number of degrees of freedom required for a faithful numerical simulation of the dynamics [27]. In addition, it provides some guidance toward the number of ordinary differential equations that would be required to reproduce the dynamics. It should be emphasized that the identification of the underlying modes remains a difficult and open challenge. However, the variation of the fractal dimension with system size in the regime of extensive chaos has been used to yield a chaotic length scale [10,14,15,33].

It has been suggested that the Lyapunov vectors associated with the large positive Lyapunov exponents may not be as significant in the long-time dynamics as the Lyapunov vectors associated with the Lyapunov exponents near zero (cf. Ref. [34]). The dynamics of the vectors associated with the large exponents represent fast dynamics where the dynamics of the vectors associated with Lyapunov exponents near zero represent much longer-lived dynamics. These slower dynamics have often been referred to as the hydrodynamic modes. The spatial features of the hydrodynamic modes are inaccessible to the Gram-Schmidt Lyapunov vectors yet are potentially accessible to the covariant Lyapunov vector approach.

In this paper, we use the covariant Lyapunov vectors to explore the chaotic dynamics of Rayleigh-Bénard convection.

We highlight that this is the first investigation using covariant Lyapunov vectors of a high-dimensional chaotic system that is experimentally accessible in the laboratory.

The remainder of the paper is organized as follows. In Sec. II we describe Rayleigh-Bénard convection and our numerical approach for computing the spectrum of covariant Lyapunov vectors for the Boussinesq equations. In Sec. III we discuss the results of our numerical exploration with the following emphasis. In Sec. III A we use the spectrum of Lyapunov exponents and the fractal dimension to quantify the complexity and high-dimensional nature of the dynamics. In Sec. III B we use the angles between pairs of covariant Lyapunov vectors to explore the degree of hyperbolicity of the dynamics and to quantify the tangled nature of the Lyapunov vectors. In Sec. III C we quantify the degree of Oseledets splitting and discuss its relation to our previous findings. In Sec. III D we explore the spatiotemporal dynamics of the spectrum of covariant Lyapunov vectors and focus upon the dominant length scales present and their degree of spatial localization. Finally, in Sec. IV we present our conclusions.

II. APPROACH

Rayleigh-Bénard convection is the fluid convection that results when a shallow layer of fluid is heated uniformly from below in a gravitational field. The dynamics are governed by the Boussinesq equations

$$\sigma^{-1}\left(\frac{\partial \mathbf{u}}{\partial t} + \mathbf{u} \cdot \nabla \mathbf{u}\right) = -\nabla p + \nabla^2 \mathbf{u} + RT\hat{\mathbf{z}} \qquad (1)$$

$$\frac{\partial T}{\partial t} + \mathbf{u} \cdot \nabla T = \nabla^2 T, \qquad (2)$$

$$\nabla \cdot \mathbf{u} = 0, \qquad (3)$$

which represent the conservation of momentum, energy, and mass, respectively. In our notation, $\mathbf{u}(x,y,z,t)$ is the fluid velocity vector, $p(x,y,z,t)$ is the pressure, and $T(x,y,z,t)$ is the temperature where (x,y,z) are Cartesian coordinates with an origin located on the lower boundary with $\hat{\mathbf{z}}$ a unit vector opposing gravity. These equations have been nondimensionalized using the vertical diffusion time of heat as the time scale, the layer depth as the length scale, and the constant temperature difference between the hot lower surface and the cool upper surface as the temperature scale. The Rayleigh number R represents the ratio of buoyancy to viscous forces. The Prandtl number σ is the ratio of the momentum and thermal diffusivities. The aspect ratio Γ is a measure of the spatial extent of the domain. For a domain with a square planform, as we will use here, the aspect ratio Γ is the ratio of the side length of the square planform to the depth of the fluid layer.

We use the no-slip boundary condition $\mathbf{u} = 0$ for the fluid motion at all material surfaces which includes the top surface, bottom surface, and the sidewalls. The lower surface is hot and is held at $T(z=0) = 1$, and the upper surface is cold and is held at a temperature $T(z=1) = 0$. The lateral sidewalls of the domain are assumed to be perfectly insulating. which can be represented as $\nabla \cdot T\hat{\mathbf{n}} = 0$, where $\hat{\mathbf{n}}$ is an outward pointing unit normal.

We compute the covariant Lyapunov vectors using the approach given by Ginelli *et al.* [22]. In essence, one first

computes the Gram-Schmidt vectors using a forward-time evolution of the tangent-space dynamics using the methods described in Refs. [10,11,17]. These Gram-Schmidt vectors are then used to compute the tangent-space dynamics *backwards* in time under the conditions that these vectors are confined to a suitable subspace. In the long-time limit the backward time evolution of these confined vectors converge to the covariant Lyapunov vectors.

In the following we provide only the essential details of how we implement this approach for the Boussinesq equations; for more details of the general approach we refer the reader to Ref. [22]. The tangent-space equations are given by a linearization of the dynamics about the Boussinesq equations. We will represent this as

$$\sigma^{-1}(\partial_t \delta \mathbf{u}^{(k)} + \mathbf{u} \cdot \nabla \delta \mathbf{u}^{(k)} + \delta \mathbf{u}^{(k)} \cdot \nabla \mathbf{u})$$
$$= -\nabla \delta p^{(k)} + \nabla^2 \delta \mathbf{u}^{(k)} + R \delta T^{(k)} \hat{\mathbf{z}}, \qquad (4)$$

$$\partial_t \delta T^{(k)} + \mathbf{u} \cdot \nabla \delta T^{(k)} + \delta \mathbf{u}^{(k)} \cdot \nabla T = \nabla^2 \delta T^{(k)}, \qquad (5)$$

$$\nabla \cdot \delta \mathbf{u}^{(k)} = 0, \qquad (6)$$

where $\delta \mathbf{u}^{(k)}(x,y,z,t), \delta p^{(k)}(x,y,z,t), \delta T^{(k)}(x,y,z,t)$ are the perturbation quantities for the velocity, pressure, and temperature, respectively. The boundary conditions for the perturbation fluid velocity is $\delta \mathbf{u}^{(k)} = 0$ on all material boundaries. The boundary condition for the perturbation temperature is $\delta T^{(k)} = 0$ on the bottom and top surfaces and $\nabla \cdot \delta T^{(k)} \hat{\mathbf{n}} = 0$ on the four lateral sidewalls of the domain. In our notation, the superscript (k) represents the kth copy of the linearized equations where $k \in [1, N_\lambda]$ with N_λ the total number of tangent-space equations. One needs to evolve an additional copy of the tangent-space equations for each Lyapunov vector and Lyapunov exponent that is desired, and therefore N_λ is also the total number of Lyapunov exponents and vectors that can be calculated (in our calculations we have used $N_\lambda = 141$ unless stated otherwise).

Equations (1)–(3) can be written more succinctly as

$$\frac{d}{dt} \mathbf{H}(t) = \mathbf{F}(\mathbf{H}), \qquad (7)$$

where $\mathbf{H}(t) = [\mathbf{u}, T]$ and $\mathbf{F}(\mathbf{H})$ are $(N \times 4)$ dimensional arrays where N is the total number of spatial points used to represent the fluid. In our numerical simulations we use $N = 128 \times 128 \times 8$. Similarly, the tangent-space equations can be represented as

$$\frac{d}{dt} \delta \mathbf{H}^{(k)}(t) = \mathbf{J}[\mathbf{H}(t)] \delta \mathbf{H}^{(k)}(t), \qquad (8)$$

where $\delta \mathbf{H}^{(k)}(t) = [\delta \mathbf{u}^{(k)}(t), \delta T^{(k)}(t)]$. We point out that the pressure does not appear in $\mathbf{H}(t)$ or $\delta \mathbf{H}(t)$ since the pressure is satisfied implicitly by the conservation of mass and does not appear explicitly as a dynamical variable. The pressure $p(t)$ can be computed from $\mathbf{H}(t)$ and the perturbation pressure $\delta p(t)$ can be computed from $\delta \mathbf{H}(t)$. The Jacobian $\mathbf{J}$ of the dynamics is given by

$$\mathbf{J}[\mathbf{H}(t)] = \frac{d\mathbf{F}}{d\mathbf{H}} \qquad (9)$$

and is evaluated at time t.

Equation (7) and N_λ copies of Eq. (8) are simultaneously integrated forward in time. The perturbation variables can be arranged into a matrix $\mathbf{G}_n$ whose columns are the perturbation vectors for each copy of the tangent space equations. The matrix $\mathbf{G}_n$ is $(4N \times N_\lambda)$ dimensional, and the subscript n indicates that this is the nth matrix computed at some discrete time t_n. The kth perturbation vector at this time is the column vector given by $\mathbf{g}_n^{(k)} = [\delta u_n^{(k)} \delta v_n^{(k)} \delta w_n^{(k)} \delta T_n^{(k)}]'$ with $4N$ elements where the prime indicates a transpose. The matrix containing these vectors as columns is then

$$\mathbf{G}_n = \left(\mathbf{g}_n^{(1)} \middle| \dots \middle| \mathbf{g}_n^{(N_\lambda)} \right). \qquad (10)$$

The vectors $\mathbf{g}_n^{(k)}$ are then periodically orthogonalized using a Gram-Schmidt procedure after a time t_N. The Gram-Schmidt procedure is equivalent to a QR decomposition of the matrix $\mathbf{G}_n$ where $\mathbf{Q}_n$ contains the orthonormalized vectors and the diagonal elements of the upper triangular matrix $\mathbf{R}_n$ contain their magnitudes. The magnitudes of the orthogonalized vectors can be used to determine the instantaneous Lyapunov exponent from

$$\tilde{\lambda}_k = \frac{1}{t_N} \ln \frac{\left|\left| \mathbf{g}_n^{(k)}(t_N) \right|\right|}{\left|\left| \mathbf{g}_n^{(k)}(0) \right|\right|}. \qquad (11)$$

The orthonormalized perturbation vectors are then evolved forward in time another t_N, and the process is repeated to compute another set of instantaneous Lyapunov exponents and Gram-Schmidt orthonormalized vectors. The average of the instantaneous Lyapunov exponents over many reorthonormalizations gives the spectrum of Lyapunov exponents λ_k,

$$\lambda_k = \frac{1}{N_0} \sum_{i=1}^{N_0} \tilde{\lambda}_k, \qquad (12)$$

where N_0 is the number of reorthonormalizations performed. The Lyapunov exponents can then be used to compute the fractal dimension D_λ using the Kaplan-Yorke formula [8].

In order to compute the kth covariant Lyapunov vector $\mathbf{v}_n^{(k)}$ at time t_n where $k \in [1, N_\lambda]$, we first integrate forward in time the tangent space dynamics to time t_m where t_m is sufficiently larger than t_n. During this forward-time integration we periodically compute and store the set of Gram-Schmidt vectors $\{\mathbf{g}_n^{(k)}\}$ using the QR decomposition approach described above. At time t_m we choose an arbitrary vector $\mathbf{u}_m^{(j)}$ that is confined to the subspace spanned by the first j Gram-Schmidt vectors $\{\mathbf{g}_m^{(l)}\}$ where $l \in [1, j]$ and evolve its tangent space dynamics *backwards* in time by inverting the upper triangular matrix $\mathbf{R}_m$. The vector $\mathbf{u}_m^{(j)}$ will converge with the backward most expanding direction to yield the covariant Lyapunov vector $\mathbf{v}_n^{(j)}$. One can then do this for all j where $j \in [1, N_\lambda]$ to yield the entire spectrum of Lyapunov vectors $\mathbf{v}_n^{(k)}$. The vector $\mathbf{v}_n^{(k)}$ is independent of t_m as long as t_m is sufficiently larger than t_n. The vector $\mathbf{v}_n^{(k)}$ is covariant with the dynamics in the sense that its magnitude will expand exponentially with an exponent of λ_k in the forward time direction and contract exponentially with an exponent of $-\lambda_k$ in the backward time direction. Therefore, in order to calculate N_λ covariant Lyapunov vectors at time t_n we need to integrate N_λ vectors $\mathbf{u}_n^{(k)}$ backwards in time to yield the $\mathbf{v}_n^{(k)}$.

Our general approach for integrating Eqs. (1)–(3) is based upon the finite-difference algorithm developed by Chiam *et al.* [35] to explore convection problems [36]. In our calculations we simultaneously integrate Eqs. (1)–(3) with N_λ copies of Eqs. (4)–(6). In order to facilitate the simultaneous computation of many Lyapunov vectors the algorithm has been parallelized such that each computation of the linearized equations is done on a separate processor. The coupling between the numerical solution of the nonlinear fluid equations and the N_λ tangent space equations is one-way toward the tangent space equations. However, there are periodic global communication requirements whenever a reorthogonalization is required.

In our numerical simulations we use an aspect ratio of $\Gamma = 16$ and a uniform numerical spatial grid size of $\Delta x = \Delta y = \Delta z = 1/8$ in all directions. The Prandtl number is $\sigma = 1$, and we have explored the range of Rayleigh numbers given by $4000 \leqslant R \leqslant 9000$, which all yield chaotic flow fields. In all cases, we have used a uniform numerical time step of $\Delta t = 0.001$.

Our numerical procedure is the following. We first run a long-time numerical simulation of Eqs. (1)–(3) so initial transients can decay to allow the chaotic dynamics to approach the attractor in phase space. It has been suggested in the literature that this time scale should be on the order of the time for heat to diffuse horizontally from the center of the domain to a sidewall [37]. This is also in qualitative agreement with previous calculations of the fractal dimension for chaotic Rayleigh-Bénard convection in large domains [10,17,20].

In our nondimensional units the horizontal diffusion time is given by $\tau_H = \Gamma^2/4$. In light of this, we first evolve the flow field forward in time for a time of $16\tau_H$ prior to computing the Lyapunov vectors. At this time we compute the N_λ Gram-Schmidt orthogonal Lyapunov vectors forward in time for a duration of $4\tau_H$. We compute a set of orthogonal Lyapunov vectors every 10 time steps. We then integrate the tangent space equations backwards in time for approximately 20 time units using the algorithm of Ginelli *et al.* [22] to compute the converged N_λ covariant Lyapunov vectors. We then continue to numerically integrate the N_λ covariant Lyapunov vectors backward in time for approximately 150 time units in order to generate the Lyapunov vector data used in our analysis.

We have run numerous numerical tests, including spatial and temporal convergence tests, to ensure the accuracy and repeatability of the results presented. We have also found that the statistics of our results are independent of the random initial conditions used.

III. RESULTS AND DISCUSSION

Typical chaotic flow field patterns are shown in Fig. 1 for the cases of $R = \{4000, 5000, 7000, 9000\}$. The color contours are of the temperature field at the horizontal midplane ($z = 1/2$) where red (light) is hot rising fluid and blue (dark) is cool falling fluid. The patterns are composed of convection rolls and different defect structures that interact rapidly in time with characteristic time scales less than one time unit. Although the patterns contain spiral and target structures the dynamics are dominated by rapid roll pinch-off events that occur frequently throughout the domain. The bottom right corner of the pattern
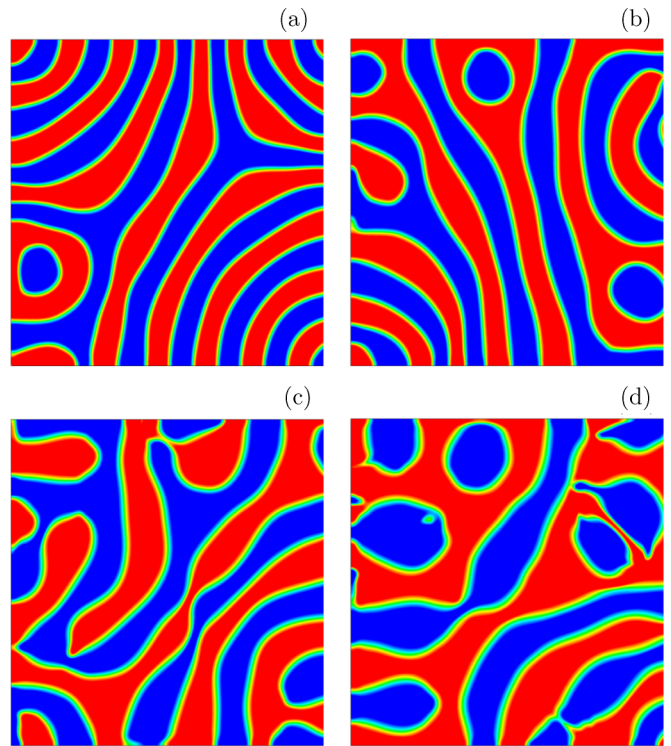

FIG. 1. Typical flow field patterns of chaotic Rayleigh-Bénard convection from numerical simulation. Contours of the temperature field at the horizontal midplane ($z = 1/2$) are shown where red (light) is hot rising fluid and blue (dark) is cold falling fluid. (a) $R = 4000$, (b) $R = 5000$, (c) $R = 7000$, and (d) $R = 9000$. The remaining simulation parameters are $\sigma = 1$ and $\Gamma = 16$.

for $R = 4000$ illustrates a wall focus, which is a typical feature of convection patterns in domains with rectangular or square cross sections.

If the domain were larger ($\Gamma \gtrsim 40$), the dynamics would be that of spiral defect chaos (cf. Ref. [35]). For the domain we explore here, there are complex interactions between the bulk dynamics, which occurs several roll depths away and greater from the sidewalls, with dynamics that are strongly influenced by the sidewalls. In our description, the width of a single convection roll is approximately unity.

It would be interesting to explore the dynamics of a larger domain; however, it is currently beyond the reach of our computational resources. We point out that for the aspect ratio chosen of $\Gamma = 16$ the dynamics are expected to be in the regime that is extensively chaotic [20]. As the Rayleigh number is increased in our simulations the time scale of the dynamics decreases, the number and frequency of local defects increases, and the spatial scale of the defect structures becomes finer.

A. Lyapunov exponents and the fractal dimension

The spectrum of the Lyapunov exponents λ_k given by Eq. (12) is shown in Fig. 2 for $4000 \leqslant R \leqslant 9000$. The leading order Lyapunov exponent $\lambda_1 > 0$ for all cases explored, indicating that the dynamics are chaotic as expected. The Lyapunov spectra appear to belong to two different groups. For the smaller Rayleigh numbers, $4000 \leqslant R \leqslant 6000$, the
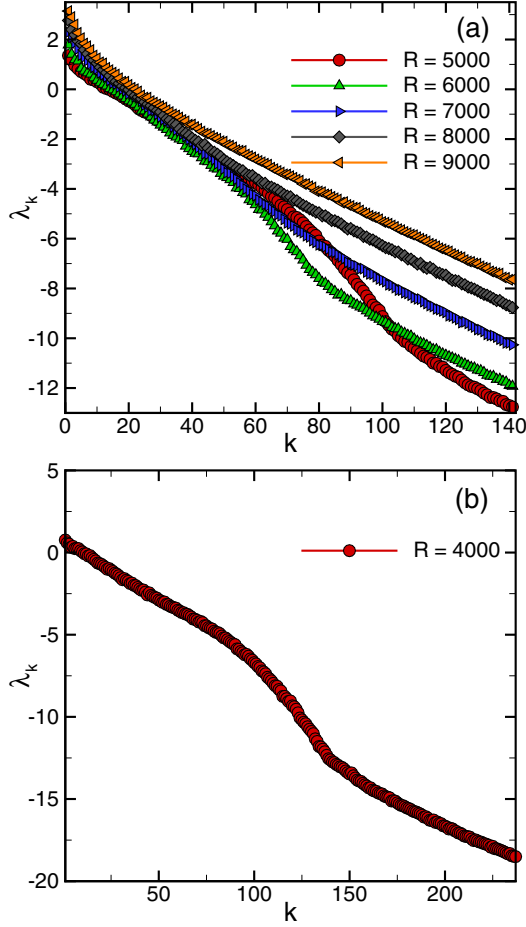
FIG. 2. The spectrum of Lyapunov exponents λ_k where $k = 1, \ldots, N_\lambda$. In all cases $\lambda_1 > 0$ indicating chaotic dynamics. (a) Results for $R = \{5000, 6000, 7000, 8000, 9000\}$ where $N_\lambda = 141$. (b) Results for $R = 4000$ where $N_\lambda = 237$. The standard deviation of the fluctuations of the Lyapunov exponents about its long-time mean value is represented by the size of the data symbols.

Lyapunov spectra contain two linear regimes separated by an elbow region with a larger negative slope. In order to resolve the elbow region for $R = 4000$ we needed to use $N_\lambda = 237$, which is shown in Fig. 2(b). For the larger Rayleigh numbers $7000 \leqslant R \leqslant 9000$ the spectra do not include the elbow region, and they all decrease uniformly with a linear dependence for increasing k. The size of the symbols used in the plot represents the size of the error in these calculations as determined by the standard deviation of the fluctuations in time of the exponent about its long-time mean value.

The variation of the fractal dimension D_λ with the Rayleigh number R is shown in Fig. 3(b). As expected, the magnitude of the fractal dimension increases with increasing Rayleigh number [10]. For these results the fractal dimension increases linearly with the Rayleigh number as indicated by the solid line, which is a curve fit through the data using $D_\lambda = 0.005R - 1.2$. This is in contrast to the $D_\lambda \propto R^4$ dependence found in Ref. [10] for similarly sized domains but with a cylindrical planform. This suggests the importance of the lateral boundaries upon the dynamics for these intermediate aspect-ratio systems with cylindrical and square planforms.
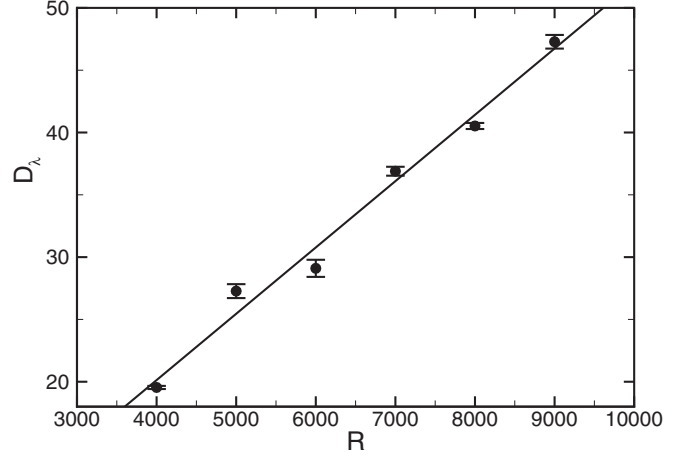

FIG. 3. The variation of the fractal dimension D_λ with Rayleigh number R. The solid line is a linear curve fit through the data given by $D_\lambda = 0.005R - 1.2$. The error bars represent the standard deviation of the fluctuations in the fractal dimension about its long-time mean value.

We also point out that these curve fits are over a very limited range of the Rayleigh number, which may also limit their range of validity.

The fractal dimension can be used as an estimate of the dimension required, or the active number of degrees of freedom on average, to describe the attractor of the dynamics in phase space [6,9]. For example, this indicates that the strange attractor describing the chaotic convection for $R = 9000$ has on the order of 50 active degrees of freedom, on average.

B. The angles between covariant Lyapunov vectors

The results presented in Figs. 2–3 depend only upon the values of the Lyapunov exponents λ_k, which can be computed using the orthogonal Gram-Schmidt Lyapunov vectors $\mathbf{g}_n^{(k)}$. A significant advantage of the covariant Lyapunov vectors is that one can quantify the angles $\phi_{i,j}$ between the vectors $\mathbf{v}_n^{(i)}$ and $\mathbf{v}_n^{(j)}$ in the tangent space.

In Fig. 4 we show the angle between several pairs of covariant Lyapunov vectors for $R = 5000$. The angle is a function of time, and therefore we plot the probability density function. When computing the probability density function we have used 10^4 samples, where each sample is acquired every 0.01 time units for a total duration of 100. We consider positive angles to be equivalent to negative angles, and we therefore represent angle measurements only over the range $\theta \in [0, \pi]$ where we have used a total of 60 bins.

Figure 4(a) shows the probability density function of the angle between neighboring pairs of vectors. The pair $(2,3)$ is for rapidly growing vectors, and the remaining pairs are for rapidly contracting vectors. The results indicate significant probability across the entire range of angle. Our results do not show a significant difference in the angle between rapidly growing and contracting vectors. For example, the pairs $(2,3)$ and $(127,128)$ yield a similar distribution that suggests that these pairs are quite tangled as illustrated by the significant probability for angles near zero. This is the
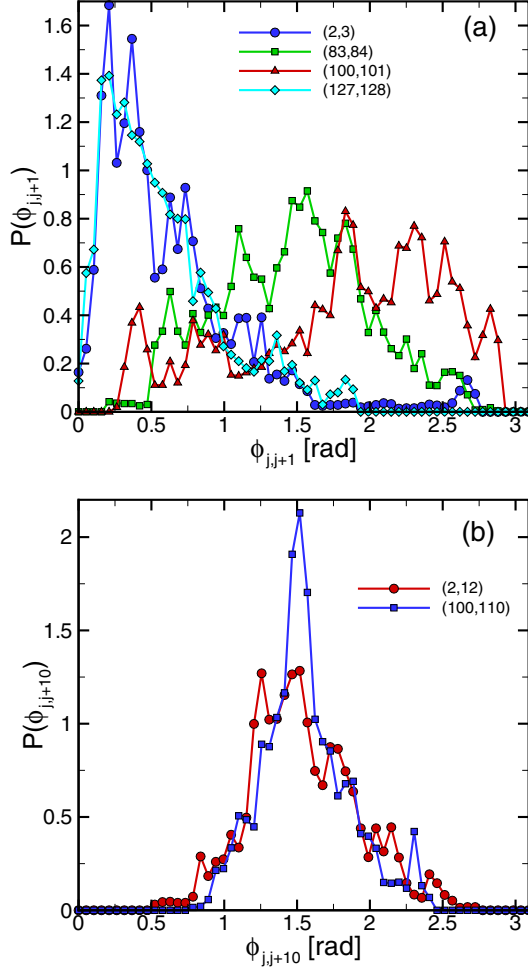
FIG. 4. (a) The variation of the probability density function of the angle between pairs of covariant Lyapunov vectors. The specific pairs (j_1, j_2) shown are $(2,3), (83,84), (100,101)$, and $(127,128)$. (b) The variation for pairs with a separation of 10. Results are shown for $(2,12)$ and $(100,110)$. These results are for $R = 5000$ where we have used 60 bins over the range $\phi \in [0,\pi]$.
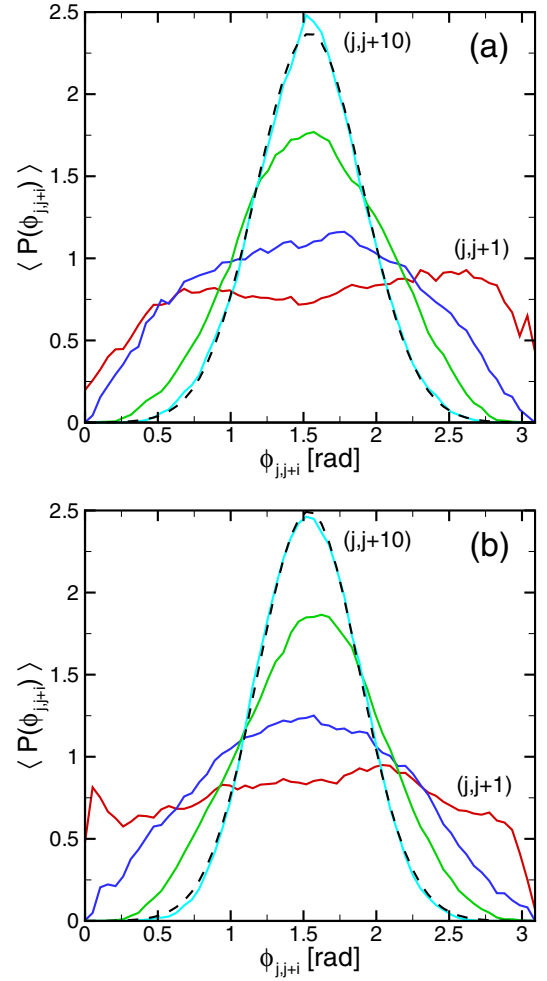

FIG. 5. The variation of the average probability density function between pairs $(j, j + i)$ of covariant Lyapunov vectors. The average is taken over all possible pairs. Results are shown for $(j, j + 1)$ (red), $(j, j + 2)$ (blue), $(j, j + 5)$ (green), and $(j, j + 10)$ (cyan). As the distance between the pairs increases the results approach a Gaussian, which is shown as the dashed line. (a) $R = 5000$; (b) $R = 9000$.

first indication we will show that suggests the covariant Lyapunov vectors of Rayleigh-Bénard convection can not be decomposed cleanly into a region of physical modes that is followed by hyperbolically isolated or spurious modes, which has been observed in a number of simpler model systems (cf. Refs. [27,28]). We emphasize, however, that our numerical results indicate the tangled nature of the spectrum of covariant Lyapunov vectors only over the range that we have computed. It remains possible that spurious modes exist beyond the range of our current calculations. The pairs shown in Fig. 4(a) are meant to convey a representative sample of the variety of distributions found over the entire range of vectors.

On the other hand, vector pairs with a larger separation in their index do yield a consistent distribution for the probability distribution function of the angle between them. Figure 4(b) shows the angle distribution for vectors pairs with $(j, j + 10)$. Results are shown only for the two pairs $(2,12)$ and $(100,110)$; however, similar results are found for all such pairs.

A clearer picture is obtained if we take the average of the probability density function $P(\phi_{j,j+i})$ for all of the possible

vectors pairs $(j, j + i)$ for the chosen value of the pair separation i where $j = 1, \ldots N_\lambda$. This is shown in Fig. 5(a) for $R = 5000$ and in Fig. 5(b) for $R = 9000$ for the vector pair separations given by $i = 1, 2, 5, 10$. In our notation, the angle brackets $\langle \cdot \rangle$ indicate that the average is taken over all of the possible pairs for that choice of the pair separation i.

For neighboring pairs of vectors ($i = 1$) there is a significant probability density across the entire range of angle including a finite value at $\phi_{j,j+1} = \{0, \pi\}$. This indicates these vector pairs contain moments in time when the vectors are nearly tangent with one another. As shown in Fig. 5 these near tangencies are not limited to some particular range of the Lyapunov vectors but occur for vector pairs over the entire spectrum. As a result, these findings suggest that adjacent pairs of covariant Lyapunov vectors contain frequent near tangencies on average. In other words, these Lyapunov vector pairs are quite tangled, on average, over the entire spectrum that we have simulated.

For vector pairs with a separation of $i = 2$ the distribution is not flat but contains a maximum near $\phi_{j,j+1} \approx \pi/2$ and

decreases to zero at $\phi_{j,j+1} = \{0,\pi\}$. This trend continues for all pairs with a larger separation as indicated by the results for $i = 5$ and $i = 10$. The dashed line is a Gaussian curve fit to the results for the vector pairs given by $i = 10$. The results for $R = 5000$ and $R = 9000$ exhibit the same trends, and in fact, this is the case for all of the Rayleigh numbers we explored here. As the index of vector separation increases $i > 10$ the Gaussian peak continues to become sharper. The results for $i > 1$ indicate that as the index of separation increases the vector pairs become orthogonal to one another on average.

In Fig. 6 we show the time average of the angle between arbitrary pairs of Lyapunov vectors $\langle \bar{\phi}_{j_1,j_2} \rangle$ for $R = 5000$, 6000, and 7000 where $\{j_1, j_2\} = 1, \ldots, N_\lambda$. In order to clearly distinguish between vector pairs that are nearly tangent $\phi_{j_1,j_2} \approx \{0,\pi\}$ from vector pairs that are nearly orthogonal $\phi_{j_1,j_2} \approx \pi/2$ we use the angle $\bar{\phi}_{j_1,j_2} \in [0,\pi/2]$ where $\bar{\phi}_{j_1,j_2} = 0$ represents either tangency (parallel or antiparallel vectors) and $\bar{\phi}_{j_1,j_2} = \pi/2$ represents an orthogonal vector pair. Color indicates the magnitude of the angle $\bar{\phi}_{j_1,j_2}$ where blue (dark) is a small value indicating tangency and red (light) is a large value indicating orthogonality. The dark blue diagonal line from the bottom left corner to the upper right corner indicates that the vector pair composed of two copies of itself ($j_1 = j_2$) has an angle between them of exactly zero as expected. This figure is symmetric about its diagonal since $\bar{\phi}_{j_1,j_2} = \bar{\phi}_{j_2,j_1}$ by construction.

These results show that vectors with a small separation in their index are more likely to have a smaller angle between them on average. Figure 6(a) shows the results for $R = 5000$, where it is clear that the angle between vector pairs near the diagonal have a smaller angle of separation on average over the entire range of j_1 and j_2. For values of the index where $j_1 \gtrsim 112$ and $j_2 \lesssim j_1$ an interesting feature is present where the average angle becomes nearly $\pi/2$, which is shown by the dark red regions near the right edge of Fig 6(a). By symmetry, the same feature can be seen for $j_2 \gtrsim 112$ and $j_1 \lesssim j_2$ near the top edge of Fig 6(a).

Figure 6(b) shows this same type of feature for $j_1 \gtrsim 74$ when $R = 7000$. This is also present at $R = 4000$ (not shown) for $j_1 \gtrsim 132$. However, for $R = 6000$ this feature is not present as shown in Fig. 6(c). In fact, the feature is absent for all $R \geqslant 7000$ that we have explored. These results suggest that the dynamics are undergoing a transition at $R \approx 7000$.

Our results suggest that neighboring pairs of covariant Lyapunov vectors have frequent near tangencies over the entire range of vectors that we have computed. This can also be seen in Fig. 7, where we plot the probability P^* of an adjacent vector pair $(j, j+1)$ having an angle that is within 0.17 radians (10 degrees) of a tangency at either $\phi_{j,j+1} = \{0,\pi\}$. Representative results are shown for $R = 5000$ as circles (red) and for $R = 9000$ as squares (blue). The probability of near tangencies occurring is present over the entire range of the vector index j. Similar results are found for all of the Rayleigh numbers we have explored. This further supports the idea that the covariant Lyapunov vectors are tangled through frequent near tangencies with neighboring vectors.

It is insightful to use the covariant Lyapunov vectors $\mathbf{v}_n^{(k)}$ to quantify the expanding and contracting subspaces in the tangent space. The expanding Lyapunov vectors, $\mathbf{v}_n^{(k)}$ where $\lambda_k > 0$, form a basis that spans the local unstable manifold E_n^u.
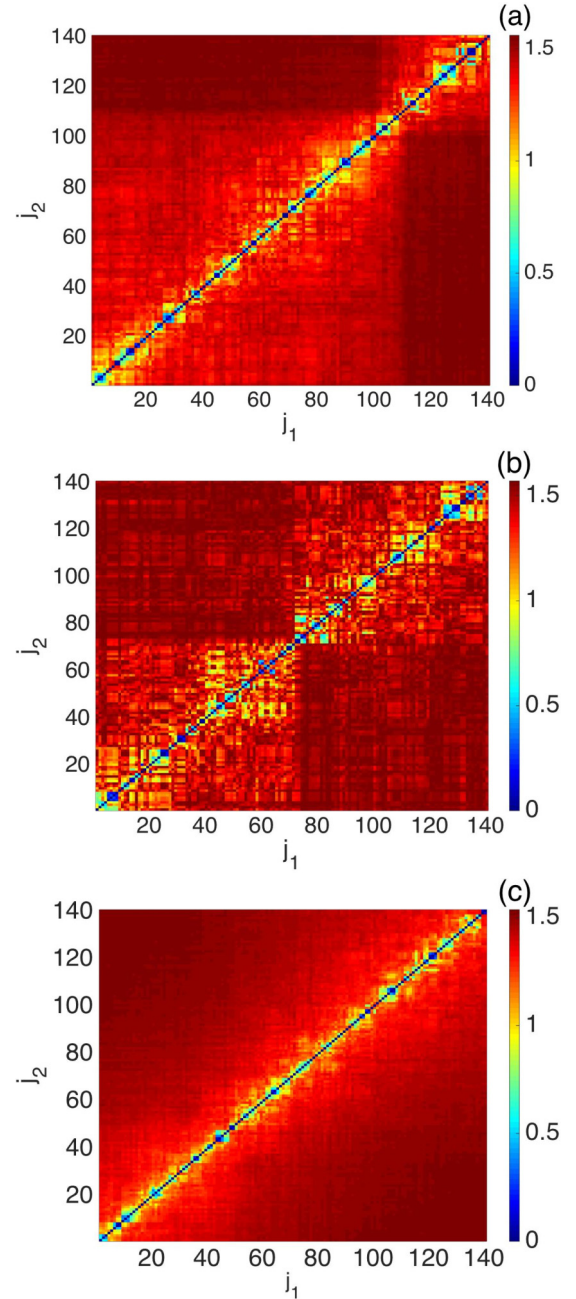

FIG. 6. The time average of the magnitude of the angle $\langle \bar{\phi}_{j_1,j_2} \rangle$ between arbitrary pairs of covariant Lyapunov vectors $\mathbf{v}_n^{(j_1)}$ and $\mathbf{v}_n^{(j_2)}$. Color indicates angle measured in radians where $\bar{\phi}_{j_1,j_2} \in \{0,\pi/2\}$ with red (light) representing large angles and blue (dark) representing small angles. (a) $R = 5000$, (b) $R = 6000$, (c) $R = 7000$.

Similarly, the contracting Lyapunov vectors $\mathbf{v}_n^{(k)}$ where $\lambda_k < 0$, form a basis that spans the local stable manifold E_n^s. The angle between the unstable and stable manifold is very important to many theoretical descriptions of the dynamics. We are interested in the minimum angle, or principal angle θ, between these two linear subspaces, which is computed using linear combinations of the corresponding vectors [30,38]. Dynamical systems where the principal angle is never zero are referred to as hyperbolic.
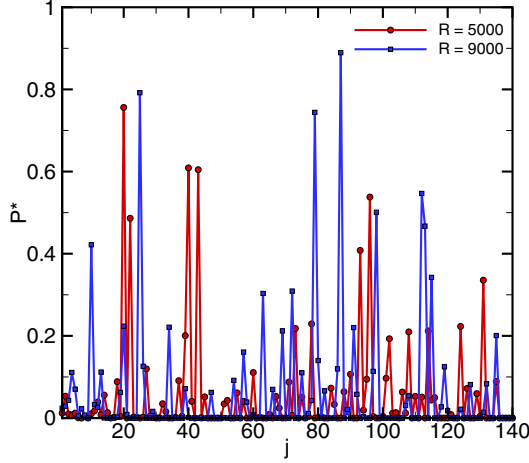
FIG. 7. The probability P^* of near tangencies for pairs of covariant Lyapunov vectors. At each point j the value of P^* is the probability of the magnitude of the angle between the pair $(j, j+1)$ to be $\phi_{(j,j+1)} \lesssim 10$ degrees. $R = 5000$ (red, circles), $R = 9000$ (blue, squares).

In Fig. 8 we show the probability density function of the principal angle $P(\theta)$ over the range of $\theta \in [0, \pi/4]$ where we have used 40 bins. One of the Lyapunov exponents must be exactly zero for autonomous dynamical systems such as the Boussinesq equations (cf. Ref. [39]). As a result, we do not include the covariant Lyapunov vector associated with this zero Lyapunov exponent in our computations of the principal angle [30].

For all of our results shown in Fig. 8, there is significant probability density at small angles $\theta \lesssim 0.2$. As the Rayleigh number is increased, the general trend is that the probability distribution moves toward even smaller angles. In order to visualize this trend, Fig. 8(b) shows the same results over the smaller range of angles $\theta \in [0, 0.1]$. Our results show that for all of the Rayleigh numbers explored here the dynamics are nonhyperbolic, as indicated by the finite probability of the principal angle at $\theta = 0$. Furthermore, the probability at zero angle increases with increasing values of the Rayleigh number, indicating that the dynamics become more nonhyperbolic as the system is driven further from equilibrium. This is in contrast to hyperbolic dynamics which would yield an angle distribution that is bounded away from zero or π indicating the absence of any near tangencies [27].

C. The domination of Oseledets splitting

The domination of Oseledets splitting (DOS) can be used to further quantify the Lyapunov vectors. We can use this idea with statistics of the instantaneous Lyapunov exponents $\tilde{\lambda}_j$, where we compute a time average of the instantaneous Lyapunov exponent over a time interval of τ, to provide some additional insights. We will denote this finite-time Lyapunov exponent as $\tilde{\lambda}_j^\tau$. We point out that the instantaneous Lyapunov exponents used here represent the expansion and contraction rates of the covariant Lyapunov vectors and are not based upon the dynamics of the Gram-Schmidt orthogonalized Lyapunov vectors.
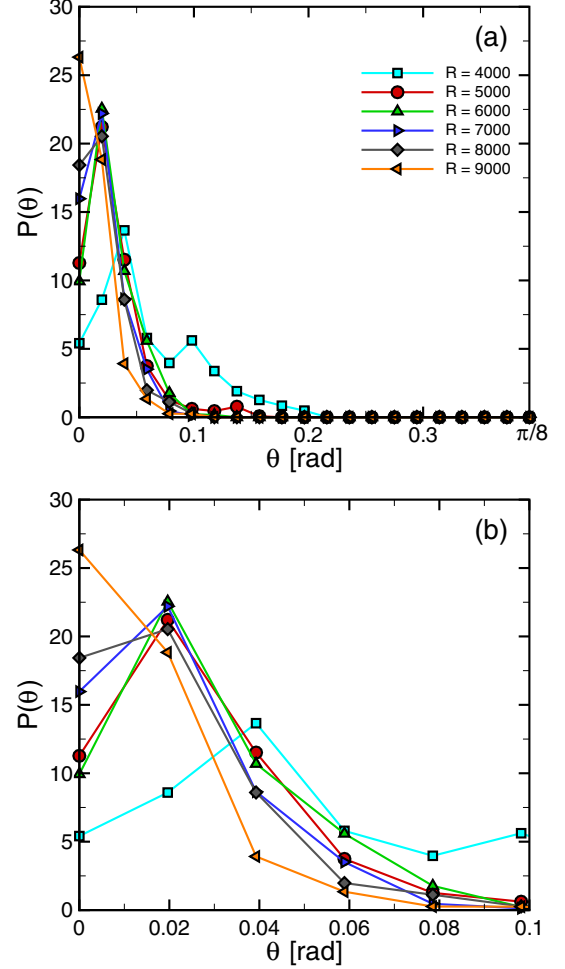

FIG. 8. (a) The variation of the probability density function of the principal angle $P(\theta)$ where the principal angle θ is the smallest angle between the stable and unstable subspaces. These results are computed using 40 bins for $\theta \in [0, \pi/4]$. (b) A close-up of the results for small θ. As the Rayleigh number is increased there is an increase in the probability at small angles.

The Oseledets splitting is dominating if $\tilde{\lambda}_{j_1}^\tau > \tilde{\lambda}_{j_2}^\tau$ for all t such that $\tau > \tau_0$ where $j_2 > j_1$ and τ_0 is a value that must be determined by trial and error. When the Oseledec splitting is dominating, it has been shown that this indicates the absence of any tangencies between the vectors [40,41]. Following the conventions used in Ref. [27] we define

$$\Delta\lambda_{j_1,j_2}^\tau(t) = \tilde{\lambda}_{j_1}^\tau(t) - \tilde{\lambda}_{j_2}^\tau(t) \qquad (13)$$

and then compute the amount of violation of the Oseledets splitting as

$$\nu_{j_1,j_2}^\tau = \langle 1 - \mathcal{H}[\Delta\lambda_{j_1,j_2}^\tau(t)]\rangle, \qquad (14)$$

where $\mathcal{H}$ is the step function and the angle brackets indicate a time average. Therefore $\nu_{j_1,j_2}^\tau \in [0,1]$ where $\nu_{j_1,j_2}^\tau = 0$ is the limit of no violation for all time and $\nu_{j_1,j_2}^\tau = 1$ is the limit of violation occurring for all time.

Figure 9 shows the degree of violation of Oseledets splitting for arbitrary pairs of covariant Lyapunov vectors where (a) is for $R = 5000$ and (b) is for $R = 9000$. Rather than plotting
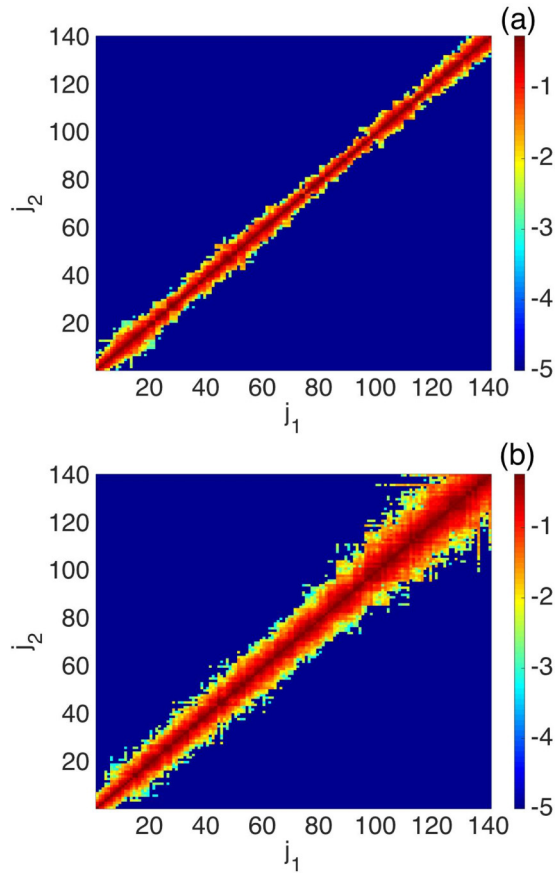
FIG. 9. The degree of violation of Oseledets splitting between arbitrary pairs (j_1, j_2) of covariant Lyapunov vectors plotted on a logarithmic scale. Color contours represent the magnitude of $\ln(\nu^{\tau}_{j_1, j_2})$ where red (light) indicates pairs with a large degree of violation and blue (dark) indicates pairs with a small a degree of violation. (a) $R = 5000$, (b) $R = 9000$.

the violation $\nu^{\tau}_{j_1, j_2}$ it is more convenient to plot its logarithm $\ln(\nu^{\tau}_{j_1, j_2})$. Red (light) regions indicate vector pairs that exhibit a significant amount of violation and blue (dark) regions indicate vector pairs with very little violation.

Figure 9 indicates the presence of significant violations for vector pairs whose index of separation i is not very large. For example, in Fig. 9(a) nearly all of the violation is contained within a band of $i \lesssim 5$ where $j_2 = j_1 + i$. In other words, i represents the required increase in the vector index away from the diagonal that one must consider in order to yield small values of the violation.

There is a finite band of violation for all vector pairs about the diagonal. This illustrates the lack of any hyperbolically isolated modes, which would appear as red (light) pixels along the diagonal with blue (dark) pixels immediately adjacent. This is another indication that the dynamics of Rayleigh-Bénard convection are composed many tangled modes with frequent near tangencies.

A similar trend emerges for $R = 9000$, shown in Fig. 9(b). Overall, the amount of violation has increased when compared with the results for $R = 5000$. In addition, the amount of violation increases as j_1 increases. The band of the violation about the diagonal increases as one goes from the bottom left to

the upper right of Fig. 9(b). For example, significant violations exist for $i \approx 5$ for $j_1 \approx 10$ and $j_2 = j_1 + i$ where i increases to $i \approx 12$ for $j_1 \approx 120$.

D. The spatiotemporal features of the covariant Lyapunov vectors

The covariant Lyapunov vectors can also be used to yield information regarding the locations in space that are significantly adding to the overal disorder of the flow field. In all previous results on Rayleigh-Bénard convection this has been possible only for the leading order Lyapunov vector [10,17–20].

In Fig. 10 we show the spatial variation of three different covariant Lyapunov vectors at the same instant of time for $R = 5000$ (top row) and for $R = 9000$ (bottom row). In all cases, we are plotting the value of the perturbation temperature $\delta T^{(j)}(x, y, z = 1/2)$ as a representation of the jth Lyapunov vector at the horizontal midplane where red (light) contours indicate large positive values and blue (dark) contours indicate large negative values. The black solid lines indicate the pattern of convection rolls.

The three Lyapunov vectors shown in Figs. 10(a)–10(c) have been chosen as representative examples to illustrate the spatial variation of the vectors. Figure 10(a) shows results for $j = 1$ and represents the case of rapidly expanding vectors ($\lambda_1 > 0$). Figure 10(b) is for $j = 12$ and represents the case where the vectors are not undergoing significant expansion of contraction ($\lambda_{12} \approx 0$). In fact, λ_{12} is the Lyapunov exponent whose value is closest to zero, on average, within the precision of our calculations for these parameters. Last, Fig. 10(c) is for $j = 120$ and illustrates our results for rapidly contracting vectors ($\lambda_{120} \ll 0$).
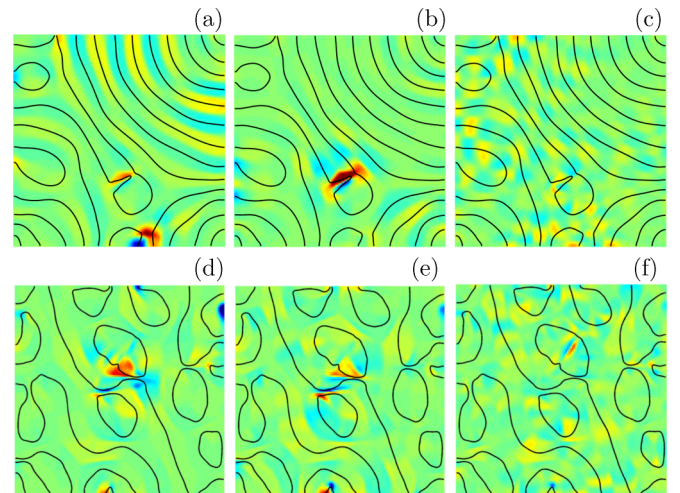

FIG. 10. The spatial variation of the jth covariant Lyapunov vector. The top row is for $R = 5000$ at time $t = 1168$ where (a) $j = 1$, (b) $j = 12$, (c) $j = 120$. The bottom row is for $R = 9000$ at $t = 1823$ where (d) $j = 1$, (e) $j = 21$, (f) $j = 120$. Color contours indicate the value of the perturbation temperature field $\delta T^{(j)}$ at the horizontal midplane ($z = 1/2$) where red (light) is a large positive value and blue (dark) is a large negative value. The black solid lines indicate the location of the convection rolls for reference.

Figure 10(a) illustrates that the leading order Lyapunov vector has large values in regions where roll pinch-off events occur. At the instant of time shown in Fig. 10(a) there are two localized regions where the magnitude of the Lyapunov vector is large. Near the center of the domain the Lyapunov vector is large near the region where a roll pinch-off is about to occur. Near the bottom of the domain there is another region of large Lyapunov vector where a roll pinch-off event just occurred a short time earlier. Similar images are found for all of the Lyapunov vectors with positive Lyapunov exponents.

For the Lyapunov vector shown in Fig. 10(b) where $\lambda_{12} \approx 0$ there remains a large magnitude near the roll pinch-off event in the central region of the domain. However, an additional feature of interest is now apparent, namely, a weak structure with a checkerboard-type pattern. For rapidly contracting Lyapunov vectors, as shown in Fig. 10(c) for $j = 120$, the magnitude of the vector near the roll pinch-offs is diminished with an increase in the magnitude of the spatially distributed checkerboard pattern.

Figures 10(d)–10(f) illustrate the spatial variation of the Lyapunov vectors for $R = 9000$ where $j = 1$ (d), $j = 21$ (e), and $j = 120$ (f). These values of the index j were chosen to represent the same cases just discussed for panels (a)–(c). For $R = 9000, \lambda_{21}$ is the Lyapunov exponent whose magnitude is closest to zero, on average, within the precision of our calculations. The general features of the Lyapunov vectors shown in panels (d)–(f) are quite similar to what is found in panels (a)–(c). In particular, the Lyapunov vectors that correspond to $\lambda_j \gtrsim 0$ show large values that are quite localized around defect structures that transitions to a more spatially distributed pattern for Lyapunov vectors where $\lambda_j \ll 0$.

Overall, these trends in the spatial dynamics of the Lyapunov vector suggest the presence of two spatial features of interest. For vectors with positive Lyapunov exponents the magnitude of the vector is large near the rapid creation and annihilation of defects that often involve roll pinch-off events. For Lyapunov vectors with exponents near zero there is an emergence of a weak spatially distributed checkerboard pattern which coexists with the localized large magnitudes near the defect events. As the Lyapunov exponents become more negative the relative importance of the checkerboard pattern begins to dominate the spatial variation of the Lyapunov vectors.

In order to explore this further we plot the spatial power spectrum of the Lyapunov vectors in Fig. 11 for (a) $R = 5000$ and for (b) $R = 9000$. Figure 11 shows the time average of the azimuthally averaged power spectral density of the covariant Lyapunov vectors where j is the index of the vector, and q is the wave number of the spatial power spectrum. Color contours indicate the magnitude of the power spectra with (red) light representing large values and blue (dark) representing small values.

In Fig. 11(a) there is significant power localized around a wave number of approximately 2 for small j where $j \lesssim 20$. The time averaged value of the wave number of the flow field [see Fig. 1(b) for a typical flow field image] found using the structure factor [1] for this value of the Rayleigh number is also approximately 2. This indicates that the spatial length scale of the Lyapunov vector is roughly the same as that of the flow field wavelength. This feature can also be seen in Fig. 10(a) where the region of large values of the Lyapunov
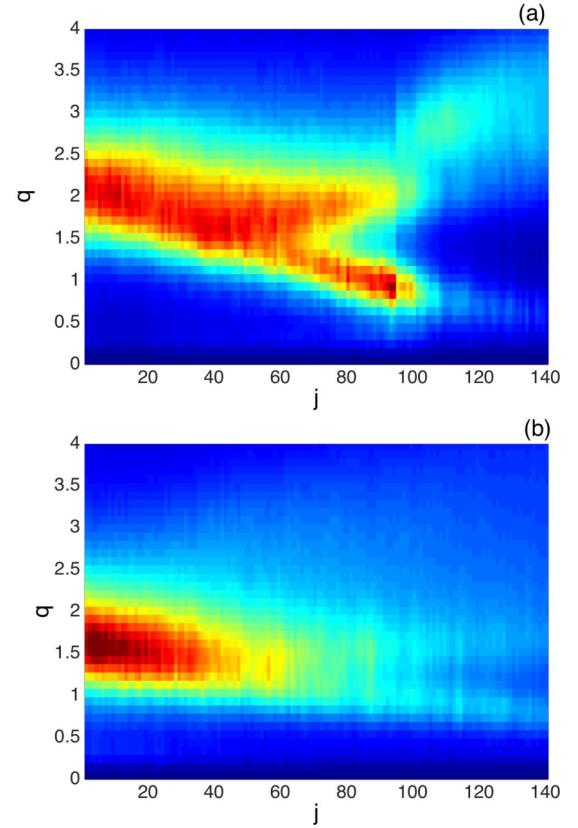

FIG. 11. Spatial power spectrum of the covariant Lyapunov vectors, q is the wave number, j is the index of the covariant Lyapunov vector, and color represents the magnitude of the power spectrum where red (light) is a large value and blue (dark) is a small value. (a) $R = 5000$, (b) $R = 9000$.

vector are approximately the same size as a convection roll wavelength. In addition to localized regions of large magnitude of the Lyapunov vector near defect structures there is also a contribution from stripe features in the Lyapunov vector that are aligned with the convection rolls.

For increasing values of j in Fig. 11(a) the power remains localized around a wave number of $q \approx 2$ with the wave number slightly decreasing with increasing values of j. For $j \approx 80$ there is a bifurcation to two separate branches in the spatial power spectrum indicating the presence of two length scales. An inspection of the spatial variation of the Lyapunov vector for $j \approx 80$ indicates the presence of both the localized features near the defect structures as well as a spatially distributed checkerboard pattern.

As the index j is increased beyond $j > 80$ in Fig. 11(a) the branch in the spatial power spectrum at higher values of the wave number diminishes significantly while the branch at lower wave number persists. Figure 10(c) shows the spatial variation of the Lyapunov vector for $j = 120$, which is dominated by the spatially distributed checkerboard type pattern. This suggests that the two branches in the spatial power spectrum may represent the checkerboard pattern and the localized features near defects found in the spatial variation of the Lyapunov vectors shown in Fig. 10. For large values of the index $j \gtrsim 115$ in Fig. 11(a) one is left with most all of the power in the checkerboard pattern.

Similar trends are found in Fig. 11(b) for the spatial power spectrum at $R = 9000$. The spatial power spectrum shown in Fig. 11(b) corresponds to the covariant Lyapunov vector dynamics illustrated in Figs. 10(d)–10(f). In this case, for small values of the index $j \lesssim 10$ the power is largest near a wave number of $q \approx 1.5$. Again, this wave number is similar to the wave number of the flow field pattern found using the time-averaged structure factor [see Fig. 1(d) for a flow field image]. As the index j increases, the region of large power in the spatial power spectrum moves to slightly smaller values of the wave number q. For $j \gtrsim 90$ there is a weak signature of a bifurcation in the spatial power spectrum toward a spectrum containing two maxima. Overall the bifurcation is much less pronounced when compared with the features of Fig. 11(a) for $R = 5000$.

IV. CONCLUSION

We have shown that it is now possible to compute the covariant Lyapunov vectors for large spatially extended systems that are experimentally accessible. We have used the covariant Lyapunov vectors to generate new physical insights into the spatiotemporal chaos of Rayleigh-Bénard convection. Specifically, we have shown that the chaotic dynamics of convection are nonhyperbolic, quantified the tangled nature of the spectrum of Lyapunov vectors, explored the spatiotemporal dynamics of the spectrum of Lyapunov vectors, and found a signature for the presence of two different length scales with different degrees of localization in the Lyapunov vectors. Overall, these results help to build our physical understanding of the complex dynamics of large systems that are driven far from equilibrium.

[1] M. C. Cross and P. C. Hohenberg, Pattern formation outside of equilibrium, Rev. Mod. Phys. **65**, 851 (1993).

[2] E. N. Lorenz, The predictability of a flow which possesses many scales of motion, Tellus **21**, 289 (1968).

[3] D. Ruelle and F. Takens, On the nature of turbulence, Commun. Math. Phys. **20**, 167 (1971).

[4] H. W. Hethcote, The mathematics of infectious diseases, SIAM Rev. **42**, 599 (2000).

[5] W. van Saarloos, Front propagation into unstable states, Phys. Rep. **386**, 29 (2003).

[6] D. Ruelle, Large volume limit of the distribution of characteristic exponents in turbulence, Commun. Math. Phys. **87**, 287 (1982).

[7] J.-P. Eckmann and D. Ruelle, Ergodic theory of chaos and strange attractors, Rev. Mod. Phys. **57**, 617 (1985).

[8] J. L. Kaplan and J. A. Yorke, Chaotic behavior of multidimensional difference equations, Lect. Notes Math. **730**, 204 (1979).

[9] J. D. Farmer, E. Ott, and J. A. Yorke, The dimension of chaotic attractors, Physica D **7**, 153 (1983).

[10] A. Karimi and M. R. Paul, Quantifying spatiotemporal chaos in Rayleigh-Bénard convection, Phys. Rev. E **85**, 046201 (2012).

[11] A. Wolf, J. B. Swift, H. L. Swinney, and A. Vastano, Determining Lyapunov exponents from a time series, Physica D **16**, 285 (1985).

[12] G. Benettin, L. Galgani, and J.-M. Strelcyn, Kolmogorov entropy and numerical experiments, Phys. Rev. A **14**, 2338 (1976).

[13] I. Shimada and T. Nagashima, A numerical approach to ergodic problem of dissipative dynamical systems, Prog. Theor. Phys. **61**, 1605 (1979).

[14] C. S. O'Hern, D. A. Egolf, and H. S. Greenside, Lyapunov spectral analysis of a nonequilibrium Ising-like transition, Phys. Rev. E **53**, 3374 (1996).

[15] A. Karimi and M. R. Paul, Extensive chaos in the Lorenz-96 model, Chaos **20**, 043105 (2010).

[16] S. Tajima and H. S. Greenside, Microextensive chaos of a spatially extended system, Phys. Rev. E **66**, 017205 (2002).

[17] D. A. Egolf, I. V. Melnikov, W. Pesch, and R. E. Ecke, Mechanisms of extensive spatiotemporal chaos in Rayleigh-Bénard convection, Nature (London) **404**, 733 (2000).

[18] A. Jayaraman, J. D. Scheel, H. S. Greenside, and P. F. Fischer, Characterization of the domain chaos convection state by the largest Lyapunov exponent, Phys. Rev. E **74**, 016209 (2006).

[19] J. D. Scheel and M. C. Cross, Lyapunov exponents for small aspect ratio Rayleigh-Bènard convection, Phys. Rev. E **74**, 066301 (2006).

[20] M. R. Paul, M. I. Einarsson, P. F. Fischer, and M. C. Cross, Extensive chaos in Rayleigh-Bénard convection, Phys. Rev. E **75**, 045203 (2007).

[21] V. I. Oseledec, A multiplicative ergodic theorem. Ljapunov characteristic numbers for dynamical systems, Trans. Moscow Math. Soc. **19**, 197 (1968).

[22] F. Ginelli, P. Poggi, A. Turchi, H. Chatè, R. Livi, and A. Politi, Characterizing Dynamics with Covariant Lyapunov Vectors, Phys. Rev. Lett. **99**, 130601 (2007).

[23] C. L. Wolfe and R. M. Samelson, An efficient method for recovering Lyapunov vectors from singular vectors, Tellus, Ser. A **59**, 355 (2007).

[24] D. Pazó, I. G. Szendro, J. M. López, and M. A. Rodríguez, Structure of characteristic Lyapunov vectors in spatiotemporal chaos, Phys. Rev. E **78**, 016209 (2008).

[25] I. G. Szendro, D. Pazó, M. A. Rodríguez, and J. M. López, Spatiotemporal structure of Lyapunov vectors in chaotic coupled-map lattices, Phys. Rev. E **76**, 025202 (2007).

[26] H. Yang and G. Radons, Comparison between covariant and orthogonal Lyapunov vectors, Phys. Rev. E **82**, 046204 (2010).

[27] K. A. Takeuchi, H. Yang, F. Ginelli, G. Radons, and H. Chatè, Hyperbolic decoupling of tangent space and effective dimension of dissipative systems, Phys. Rev. E **84**, 046214 (2011).

[28] H. Yang, K. A. Takeuchi, F. Ginelli, H. Chatè, and G. Radons, Hyperbolicity and the Effective Dimension of Spatially Extended Dissipative Systems, Phys. Rev. Lett. **102**, 074102 (2009).

[29] M. Inubushi, M. U. Kobayashi, S. Takehiro, and M. Yamada, Covariant Lyapunov analysis of chaotic Kolmogorov flows, Phys. Rev. E **85**, 016331 (2012).

[30] F. Ginelli, H. Chatè, R. Livi, and A. Politi, Covariant Lyapunov vectors, J. Phys. A **46**, 254005 (2013).

[31] E. Ott, *Chaos in Dynamical Systems* (Cambridge University Press, Cambridge, 1993).

[32] J. C. Robinson, Finite-dimensional behavior in dissipative partial differential equations, Chaos **5**, 330 (1995).

[33] M. P. Fishman and D. A. Egolf, Revealing the Building Blocks of Spatiotemporal Chaos: Deviations from Extensivity, Phys. Rev. Lett. **96**, 054103 (2006).

[34] H. Yang and G. Radons, Lyapunov modes in extended system, Philos. Trans. R. Soc. London A **367**, 3197 (2009).

[35] K.-H. Chiam, M. Lai, and H. S. Greenside, Efficient algorithm on a nonstaggered mesh for simulating Rayleigh-Bénard convection in a box, Phys. Rev. E **68**, 026705 (2003).

[36] A. Karimi and M. R. Paul, Length scale of a chaotic element in Rayleigh-Bénard convection, Phys. Rev. E **86**, 066212 (2012).

[37] M. C. Cross and A. C. Newell, Convection patterns in large aspect ratio systems, Physica D **10**, 299 (1984).

[38] P. V. Kuptsov and S. P. Kuznetsov, Violation of hyperbolicity in a diffusive medium with local hyperbolic attractor, Phys. Rev. E **80**, 016205 (2009).

[39] L. Sirovich and A. E. Deane, A computational study of Rayleigh-Bénard convection. Part 2. Dimension considerations, J. Fluid Mech. **222**, 251 (1991).

[40] C. Pugh, M. Shub, and A. Starkov, Stable ergodicity, Bull. Am. Math. Soc. **41**, 1 (2003).

[41] J. Bochi and M. Viani, The Lyapunov exponents of generic volume-preserving and symplectic maps, Ann. Math. **161**, 1423 (2005).